Model calculations of the response of CZT strip detectors

E. Kalemci[a], J. L. Matteson[a], R. T. Skelton[a]
P. L. Hink[b] and K. R. Slavis[b]

[a]Center for Astrophysics and Space Sciences, University of California
San Diego
9500 Gilman Dr., La Jolla, CA 92093-0424

[b]Department of Physics and McDonnell Center for the Space Sciences
Washington University
St. Louis, MO 63130

ABSTRACT

Position-sensitive CZT detectors for research in astrophysics in the five – several hundred keV range are being developed by several groups. These are very promising for large area detector arrays in coded mask imagers and small-area focal plane detectors for focusing X-ray telescopes. We have developed detectors with crossed-strip readout and optimized strip widths and gaps to improve energy resolution. A "steering electrode" is employed between the anode strips to improve charge collection. A model of charge drift in the detectors and charge induction on the electrodes has been developed to allow us to better understand these types of detectors and improve their design. The model presently accounts for the electric field within the detector, the charges' trajectories, mobility and trapping of holes and electrons, and charge induction on all electrodes including their time dependence. Additional effects are being added. The model is described and its predictions are compared with laboratory measurements. Results include (1) the dependence of anode, cathode and steering electrode signals on interaction depth, transverse (to the strips) position, electron and hole trapping, strip width and gap, and bias, (2) trajectories of charges for various anode and steering electrode bias voltages, (3) a method to improve energy resolution by using depth of interaction information, and (4) an electrode geometry and bias optimized for the improved energy resolution. In general, the model provides good agreement with the measurements.

Keywords: CdZnTe, CZT detectors, strip detectors, solid state detectors, X-ray astronomy

1. INTRODUCTION

CdZnTe (CZT), a semiconductor detector of X-rays and gamma-rays, has numerous applications in scientific and technological fields, most notably in medical imaging and high energy astrophysics. An important objective of high energy X-ray astronomy is a full sky survey at energies ~ 10 to several hundred keV at a sensitivity level that will yield many new sources.[1] These sources include ordinary objects such as stellar coronea, galaxies, cluster of galaxies as well as exotic ones, such as black holes, active galactic nuclei and neutron stars. Fundamental information on many topics in astrophysics is obtained by observing those sources in X-rays. Coded mask techniques can be used along with a detector having submillimeter position resolution and a few keV energy resolution to achieve this objective.[2] (For more information on the objectives and status of high energy astronomy, see Matteson et al.[3])

These requirements are met with CZT. It is dominated by photoelectric absorption due to high Z, and its large bandgap (~ 1.4 eV) allows room temperature operation. Its high bulk resistivity at room temperatures, $\sim 10^{11}$ Ωcm, results in low leakage currents and noise in a small detector, i.e. 1 cm^2. CZT's energy response is linear over the energy range of interest.[4] However, CZT material has poor hole transport properties. Conventional planar configuration for the detector shows low energy tailing in their spectra for energies higher than 60 keV due to incomplete hole collection. Strip or pixel detectors can eliminate this problem by virtue of the small pixel effect.[5,6]

Further author information:
E. Kalemci: E-mail: emrahk@mamacass.ucsd.edu
J. L. Matteson: E-mail: jmatteson@ucsd.edu

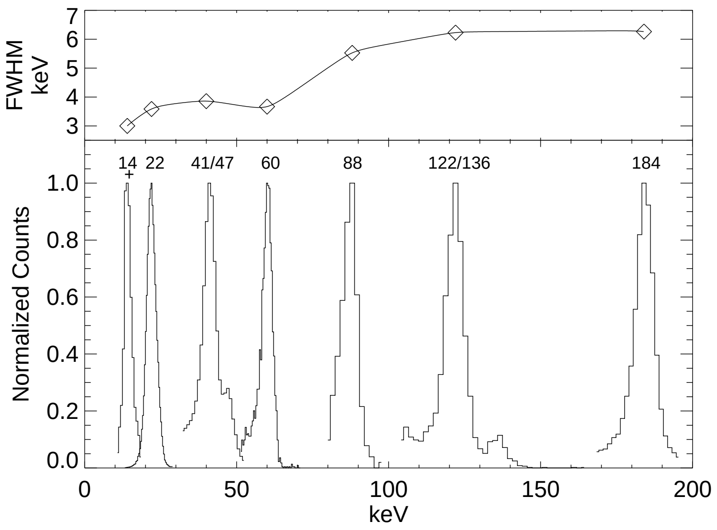

Figure 1. Line profiles and energy resolution of prototype CZT strip detector

Position-sensitive strip CZT X-Ray detectors for use in X-Ray Astronomy have been developed by UCSD and WU which have very good energy (e.g. 4.2 keV at 60 keV and 6.4 keV at 122 keV) (See Fig. 1) With lower noise electronics, such as described in Matteson et al.[7] , even better resolution can be obtained.

In order to obtain a better understanding of the performance of the detector, a modelling program was developed. The objective is to predict the spectra and the signal waveforms of X-rays interacting in a CZT strip detector. This requires determining the positions of interactions, propagating the electron-hole pairs, calculating the charges induced on electrodes and modelling pulse shaping electronics. At this time, the model does not account for X-ray interactions and electronic effects, but its calculations of charge transport and signal production are in very good agreement with the experimental measurements.

2. BASIC PRINCIPLES FOR THE MODEL

2.1. X-Ray Interactions

For the energy range of interest, $\sim$ five - several hundred keV, interactions of photons with the detector are mostly photoelectric. For example at 100 keV photoelectric cross section is $\sim$ 10 times greater than the Compton scattering cross section. At 250 keV, the cross sections are equal.

Cd and Te have K edges at $\sim 25\,\mathrm{keV}$ and $\sim 31\,\mathrm{keV}$ respectively. So an X-ray with energy greater than 25 keV can produce a photoelectron and a characteristic K X-ray. Normally, the K X-ray will be absorbed within $\sim 100\,\mu\mathrm{m}$ of the interaction position, unless the interaction is close to the physical boundaries of the detector, and it escapes. The photoelectron loses energy by creating electron-hole pairs. It will be stopped completely within a short distance, e.g., 30 μm for 100 keV X-rays This, along with thermal diffusion, causes an initial spreading of the electron-hole plasma.

2.2. Charge Transport

When bias is applied between anodes and cathodes, charges drift along the electric field lines. Up to fields of $\sim 10\,\mathrm{kV/cm}$ the drift velocity of electrons and holes are proportional to the field.[8] ($v = \mu\ E$, where μ is the mobility.) For higher fields, they drift with a constant speed. In CZT, electrons move much faster than holes and typical mobilities are $\mu_e \sim\ 1000\,\mathrm{cm^2\,V^{-1}s^{-1}}$, $\mu_h \sim\ 50\,\mathrm{cm^2\,V^{-1}s^{-1}}$, respectively.[9,10] A lower value of hole mobility, $\mu_h \sim\ 15\,\mathrm{cm^2\,V^{-1}s^{-1}}$, is also reported.[11]

2.3. Trapping and Detrapping

The charges can be trapped on their paths due to trapping sites in the crystal structure. The trapping can be quantified by trapping time τ defined as mean free drift time of carriers before trapping occurs.[12] Both electrons and holes detrap as well, which restores detector's charge neutrality. A useful quantity is the trapping length defined as: $L(x) = (\mu\,\tau)\,E(x)$. If the electric field is constant, the charge remaining as a function of distance is written as:

$$Q_{e,h}(x) = Q_{e,h}(0)\,\exp[-d/L_{e,h}(x)]. \tag{1}$$

where $Q(0)$ is the total number of electron-hole pairs created and d is the distance from the interaction site. Since holes move much slower than electrons, they are more susceptible to trapping. The typical values found in the literature for electron and hole $\mu\tau$ products are $\mu_e\tau_e \sim 3\times10^{-3}\,\mathrm{cm}^2\,/\,\mathrm{V}$, $\mu_h\tau_h \sim 1\times10^{-4}$ to $8\times10^{-6}\,\mathrm{cm}^2\,/\,\mathrm{V}$.[10,13] Those values correspond to a τ_e of around $3\,\mu$s and a τ_h of $2\,\mu$s to 160 ns respectively. For a typical field of 1000 V/cm, the corresponding trapping lengths are $L_e \sim 3$ cm and $L_h \sim$ 1 mm to 0.08 mm respectively.

Detrapping is a complicated phenomenon whose effects depend on temperature, material and pulse shaping electronics. Its details are discussed by Martini et al.[14] and by Mayer.[15]

2.4. Charge Induction

The charge induced on each electrode can be calculated by the weighting potential method,[16] $Q_{ind} = -Q(x)\,W(x)$, where $W(x)$, the weighting potential, is a number between 0 and 1, and can be obtained by solving the Laplace equation in the system where unit potential is assigned to the particular electrode and the remaining electrodes are assumed to be grounded. Electron-hole pairs separate under the applied field, and, as they drift, they induce charges on each electrode with the relation above. Because of trapping, some charges do not reach the electrodes, and the total induced charge on an electrode is a function of an interaction's position. For a planar detector, an analytic solution to total charge induction as a function of depth is given by the Hecht equation[17]:

$$Q_{ind}/Q(0) = (L_e/D)(1-\exp[-(D-x)/L_e]) + (L_h/D)(1-\exp[-x/L_h]) \tag{2}$$

where D is the detector thickness and the interaction occurs at a distance x from the cathode. Note that the Hecht equation is valid only when detrapping within the integration time is negligible. For a strip detector the induced charge can be found numerically as in this paper, or can be calculated analytically by integrating the current equation.[5,18]

For a strip or pixel detector, an anode has strong weighting potential only in its vicinity due to its small size compared to the detector size. See Fig. 7 for an example. If illumination is from the cathode side, the holes trapped near the cathodes do not affect the anode signal since there is no appreciable weighting potential. Indeed, for the energy range in interest, most of the interactions are near the cathodes. Since electrons show good transport properties, they are collected at anodes. This is "the small pixel effect". Due to this effect, strip or pixel detectors yield superior performance to planar detectors.[5,6]

3. MODELLING

By using the principles explained above, a computer simulation of a CZT detector was developed that predicts induced charge on each electrode for various geometries. It consists of two parts: (1) calculation of electric fields and weighting potentials, and (2) charge drift, trapping and calculations of induced charge using the fields and potentials. The former is done with a commercial program, MAXWELL,[19] which, for a given geometry calculates the potentials and fields and saves the values to a file. Then a C program reads those values, and drifts charges on a rectangular grid. The grid is coarse at the cathode side ($10\,\mu$m) and fine ($1\,\mu$m) near the anode side to accurately follow the trajectory. Cathodes are at the top and the electrons move down on grid points following the electric field lines. If the grid size is M, depth on the grid is z and the interaction depth is z_o, then for electrons:

- $\Delta z = M$
- $\Delta t = M/(\mu_e\,E_z)$

- $\Delta x = \mu_e \; E_x \; \Delta t$
- $L_e = \mu_e \; \tau_e \; (E_x^2 + E_z^2)^{1/2}$
- $Q(z) = Q(z-1) \; \exp(-(x^2 + M^2)^{1/2}/L_e)$ and $Q_T(z-1) = Q(z) - Q(z-1)$
- $Q_{ind} = Q(z) \; W(z) \; + \; \sum_{i=z_0}^{z-1} Q_T(i) \; W(i)$

where Q_{ind} is the induced charge on a specific electrode and $Q_T(i)$ is trapped charge at site i. A similar set of equations applies to holes. Induced charge is calculated for each electrode type.

A cautionary remark is needed here since for some geometries involving steering electrodes, E_z might change sign close to steering electrodes. Those cases must be treated carefully. (For example, for an interaction in this region, the holes prefer to drift to steering electrodes, instead of cathodes.)

The model assumes a linear field-velocity relation throughout the detector. The charges trapped are not detrapped. Point charges are used, and there is no diffusion or initial spreading of electron hole plasma. The model does not include Compton scattering and K X-rays.

4. EXPERIMENTAL SET UP

The detector modelled is a laboratory prototype which was developed to study techniques for X-ray imaging instruments such as HEXIS[7] and MARGIE.[20] There are 22 anode and 22 cathode orthogonal strips on the $12 \times 12 \times 2$ mm^3 detector. (See Fig. 2.) In addition, there are steering electrodes in between anodes to enhance the charge collection. Steering electrodes are connected to each other. Anodes and steering electrodes are 100 μm wide, cathodes are 450 μm wide, and all have 500 μm pitch. The anodes are biased at 200 V and steering electrodes at 180 V, so charges created above steering electrodes are directed to anodes. (See Fig. 3) A ceramic carrier holds the detector. The electrodes are coupled to Amptek A250 charge sensitive preamplifiers. Signals then are processed by shaping, amplifying and triggering circuits, and digitized by ADC's which give the total signal. An on-line program processes the data and builds multiple spectra according to various event selection criteria.[7,21] Off-line processing is also used.

The system also carries a planar detector with the same size as the strip detector, monitored by the same electronics. This gives an opportunity to compare the performance of strip detector to the planar detector.

An additional setup was used to measure pulse shapes from various electrodes. The detector was illuminated by X-ray sources with two Amptek A250 preamplifiers connected. Signals were recorded using a Tektronix DSA 601 four channel digital oscilloscope. The archive of those measurements includes various combinations of anodes, cathodes

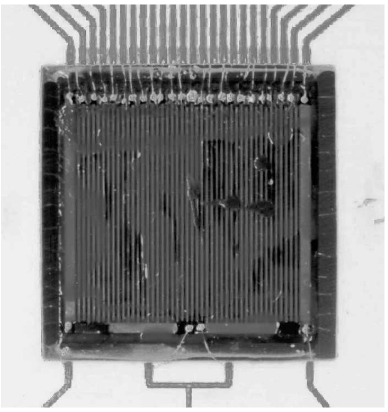

Figure 2. Prototype CZT strip detector. 22 anode strips with 500 microns pitch and 22 steering electrodes. Total size is 12x12x2 mm^3.

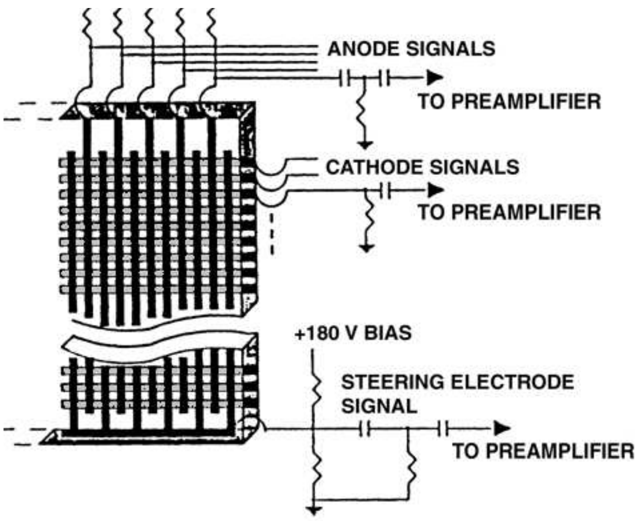

Figure 3. Detector electrode and bias network connections.

and steering electrodes. Sources used were ^{57}Co which primarily emits 122 keV γ-rays which are fully absorbed, and ^{137}Cs which emits γ-rays at 662 keV. These can Compton scatter and leave energies up to 382 keV in the detector.

To obtain transport properties, a set of measurements was made with an alpha particle source on a planar detector. The alpha beam was collimated to make it monoenergetic. The anode was coupled to an Amptek A250 preamplifier and the detector was illuminated from cathode side to determine electron transport properties. Then the bias was reversed to get hole transport properties. For bias voltages from 15 V to 210 V, the signals were recorded with the digital oscilloscope and the spectra were recorded by a ND76 Spectrum Analyzer.

5. RESULTS

5.1. TRANSPORT PROPERTIES

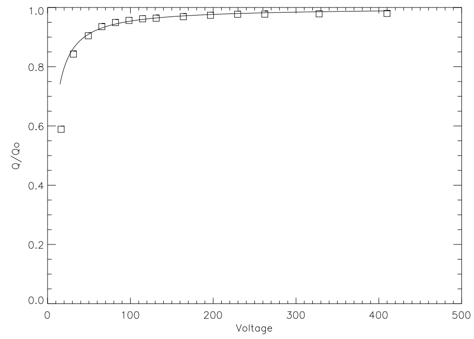

Figure 4. Measured peak height as a function of applied bias for alpha particles impinging on the cathode. Solid line is a fit to Hecht Equation, eqn(2).

The measurements done using the planar detector gave important insights. Spectra obtained from the motion of electrons had good energy resolution ($\sim$ 3% FWHM) for the electric fields greater than 1000 V/cm. The amplitudes were used to fit the Hecht equation (See Fig. 4), and a $(\mu\tau)_e$ of 5.5x10^{-6} cm s V^{-1} was obtained. For the holes however, 3 μs shaping time of the amplifier caused a severe ballistic deficit effect. The peaks were very broad, $\sim$80% at any bias. This may be due to non-uniform hole trapping and electric field.[8]

The individual signal versus time curves were also used to obtain transport parameters. The mobility of electrons was measured by using the slope of the linear part of signal vs time.[14,15] See Fig. 5 for an example. The values were between 900 and 1100 cm^2 V^{-1} s^{-1} with a mean of 960 cm^2 V^{-1} s^{-1} . But even for high biases, signal versus time curves were not completely linear, and showed a gradual non-linear increase to the maximum. This is a typical sign of detrapping[14,15] which makes the Hecht equation fit questionable. Still, it gives an effective $\mu\tau$, and determined value obtained, 5.5×10^{-6} cm s V^{-1}, is close to 6.2×10^{-6} cm s V^{-1} which resulted in the best agreement with the measurements. (Fig. 13, Sect. 5.3.)

The slope method was also applied for the holes, and an average of $\mu_h \sim 22$ cm^2 V^{-1} s^{-1} was obtained, which is smaller than usually found in the literature. Perhaps, an effective mobility was found with this method, since hole transit time (time required for carriers to tranverse the detector) may be comparable to trapping and detrapping times.[15]

5.2. TRAJECTORIES AND WEIGHTING POTENTIALS

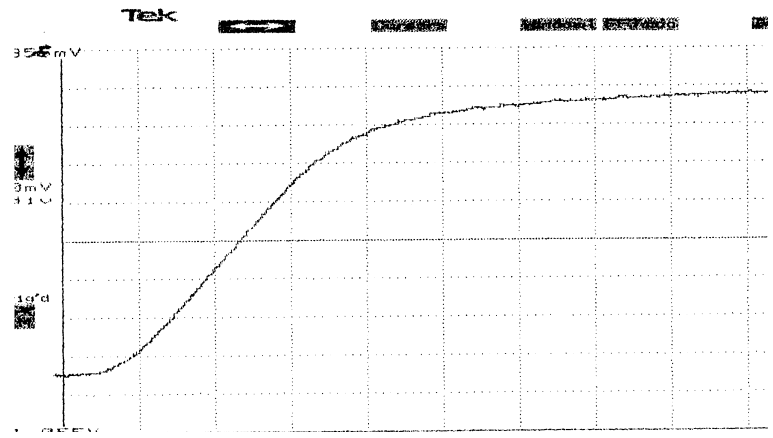

Figure 5. Signal versus time of an electrode when an alpha particle impinges on the cathode for a planar detector. The x-axis unit is 100 ns per division, and y- axis unit is 20 mV per division.

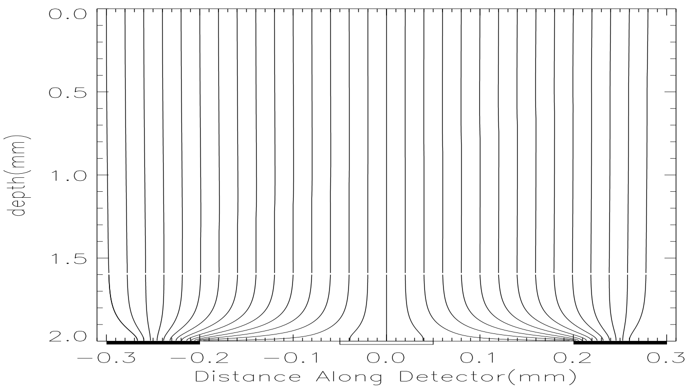

Figure 6. Model calculation of charge drift trajectories. (X- and y-axes are not scaled the same.) Filled boxes are anodes and empty boxes are steering electrodes here and in Fig. 7

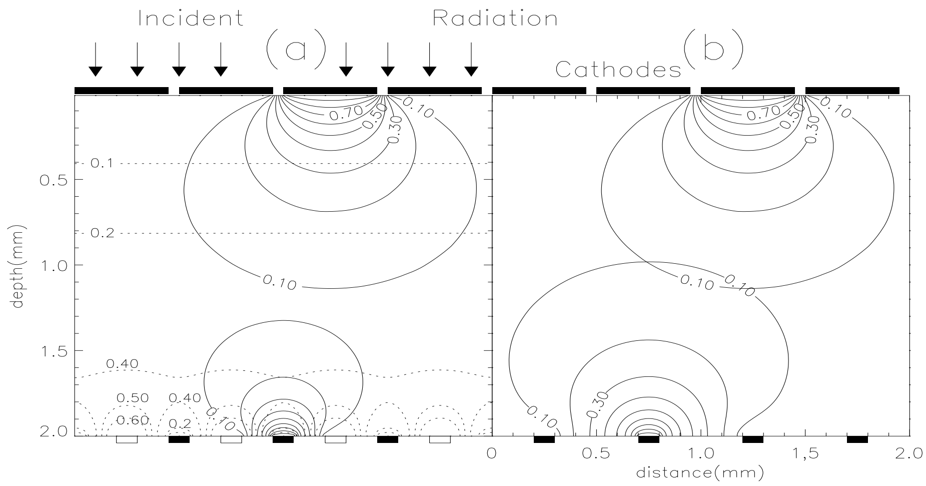

Figure 7. (a) Model calculation of weighting potential of the prototype detector. The dashed lines are steering electrodes weighting potential. (b) Model calculation of weighting potential without the steering electrode

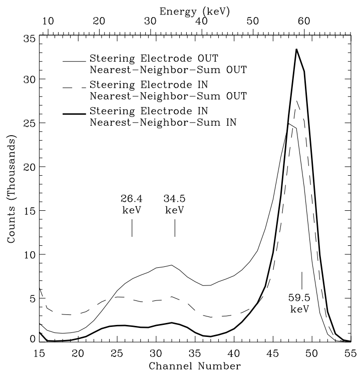

Figure 8. Effects of the steering electrode and nearest neighbor sum for an anode spectrum. Source is ^{241}Am. From Matteson et al.[2]

Results of electric field calculations are shown in Fig. 6. It is clearly seen that most of the trajectories are directed onto the anodes by the steering electrode. However, some go to the steering electrodes and the gaps. For interactions at random positons near to the cathodes, 85% go to the anodes, 10% to the steering electrode, and 5% to the gap.

Figure 7a shows weighting potential distributions of all three types of electrodes. The cathode weighting potential extends deep into the detector, e.g., $W \sim 0.1$ at a depth of 1.2 mm. Steering electrode weighting potential is also very extended, $W \sim 0.1$ at depth 0.4 mm. As discussed before, if weighting potential of an electrode is extended, signals from that electrode are affected by hole trapping. On the other hand, the weighting potential of the anodes is localized to the immediate vicinity of the anodes. Thus, the anodes benefit from the small pixel effect.

It was well established that addition of steering electrodes to the detector improved energy resolution.[2] Figure 7b explains the main reason for this. Without the steering electrodes, weighting potential of the anode extends further, reducing the small pixel effect. The effect of relative biasing is also modelled. When there is no bias between steering electrodes and anodes, 20% of the trajectories end up in the gap, which would result in incomplete charge collection. Also from the remaining 80%, half of them end up in steering electrode which does not provide position information. Fig. 8 shows the difference in spectra when there is biasing and there is no biasing.

5.3. DEPTH OF INTERACTION

Weighting potential curves clearly indicate that the amplitude of the signals is a function of depth of interaction. This effect, which causes a low energy tail due to incomplete charge collection, was studied with the model by calculating the total signals for interactions at various depths. An electron trapping length of 6 cm and hole trapping length of 0.24 mm were used. Fig. 9 shows the results. For the anodes, the response is uniform to $\pm 2\%$ for depths less than 1.7 mm. For the depth greater than 1.8 mm, the anode signal amplitude becomes lateral position dependent. Typically, useful signals are produced on several neighboring cathode strips due to trapping of holes. Fig. 10 is an example of this which shows signals of two neighboring cathodes as a function of time. For the single cathode with the largest signal, Fig. 9 shows a rapid decrease in signal with depth. When the two neighboring cathode signals are added, the depth dependence is much less severe. Therefore by adding neighboring cathode signals to the one which has the maximum signal, better spectra can be obtained (See Fig.11).

The model was tested with a series of experiments. Data were collected by flood illumination with ^{57}Co at 122 keV. For each event, the ratio of cathode to anode signal and steering electrode signal were determined. These were plotted as a scatter plot in Figure 12 along with the model predicitons. The agreement is very good. This technique was used by Slavis et al.[21] to reduce background by rejecting events which were not incident X-rays.

It has been mentioned before that cathode to anode ratio is a monotonic function of depth.[2] Relative anode signal versus cathode to anode ratio is plotted along with the model prediction. The agreement is very good, except at a very small region with high cathode to anode ratios. (See Figure 13.)

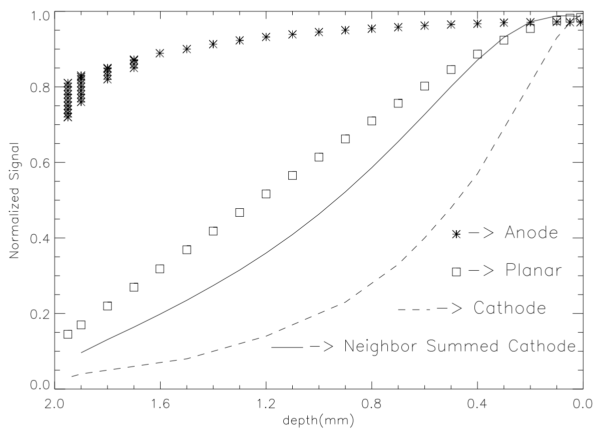

Figure 9. Model calculations of total signals at electrodes of prototype strip detector and planar detector.

The model results were used to correct for the dependence of signal on depth of interaction and thus improve energy resolution. Pulse heights were multiplied by correction factors which were obtained from the model, using the cathode to anode ratio. Results are shown in Figure 14. In the corrected spectrum, interactions deeper than 1.7 mm have been discarded. This means discarding 18% of the events for 100 keV and less than 1% for 60 keV. There is significant improvement in energy resolution. The corrected spectrum has energy resolution of 7 keV whereas the uncorrected neighbor summed spectrum has 10.5 keV energy resolution at 122 keV. For comparison, a spectrum obtained from the top 0.05 mm of the detector is also plotted. This region presumably has the best energy resolution.[22,2] There is almost no difference between two spectra. The low energy tail is eliminated and the shape is symmetric. This method can be implemented in the software very easily.

5.4. SIGNAL VERSUS TIME

Depending on the interaction position, there are various types of signal behavior of the electrodes. Several examples are shown in the following, which are modelled with following parameters: $\tau_e = 6\,\mu$s , $\mu_e = 1000\,\mathrm{cm^2\,V^{-1}\,s^{-1}}$ and $\tau_h = 645$ns and $\mu_h = 40\,\mathrm{cm^2\,V^{-1}\,s^{-1}}$. Fig.15 shows the general results for a typical interaction at $200\,\mu$m. The anode signal rises slowly until electrons reach significant weighting potential (See Fig. 7a). Then, it rises rapidly with a typical risetime of 50-70 ns. Only 3% of the electrons are trapped. On the other hand, the cathode signal increases promptly due to its extended weighting potential. This signal usually consists of two parts, (1) a rapid component due to electrons drifting away from the cathode (they move to lower weighting potential) and (2) a slow component due to holes approaching the cathodes. Charge collection is incomplete due to trapping. Fig. 15e shows a typical signal with all the features described above, measured with our setup with ^{57}Co.

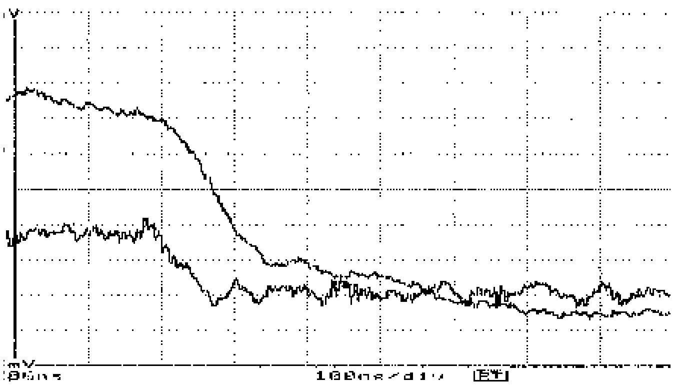

Figure 10. Typical cathode and neighboring cathode signals as a function of time. X-axis is 100 ns per division and y-axis is 1 mV per division.

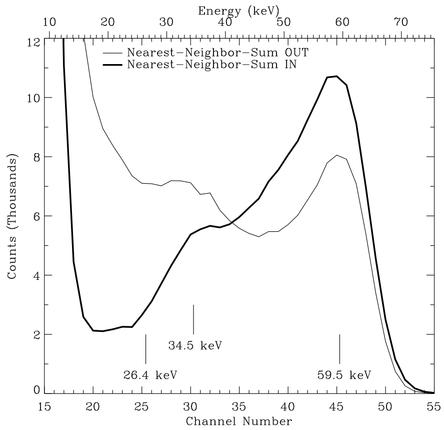

Figure 11. Effect of nearest neighbor sum for a cathode spectrum. Source is Am^{241}. From Matteson et al.[2]

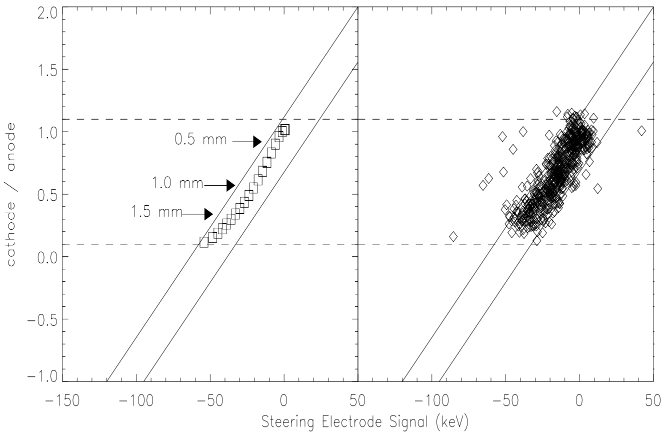

Figure 12. Modelled (left) and measured (right) depth of interaction effect on cathode to anode ratio and steering electrode signal for 122 keV X-rays.

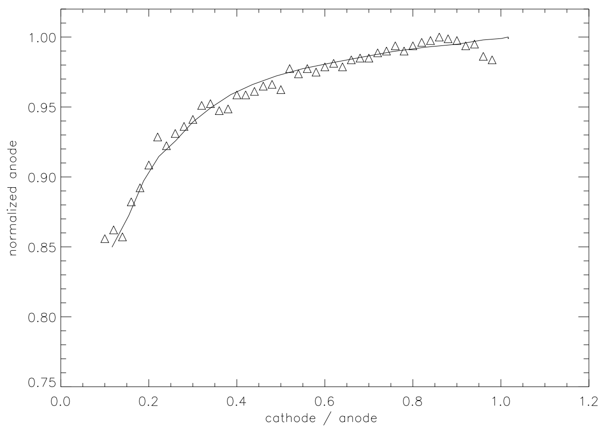

Figure 13. Anode signal versus cathode to anode ratio. Triangles are measurements for 122 keV and solid line is the model prediction.

A second example (Figure 16) illustrates the behavior of signals on the steering electrode when electrons are collected at an anode. The interaction is at $600\,\mu$m. The signal first rises rapidly but then drops to a negative value. Then it rises very slowly. To understand this, recall Fig. 7a. The weighting potential of the steering electrodes rises, down to a depth of 1.6 mm, then drops quickly to zero near the anodes. The modelled signal drops down not to zero but negative values because of trapped holes. The slow increase at the end is due to untrapped holes going away from the steering electrodes. The measurements (See Fig. 16e for a typical signal) show those properties. For the case of an event at the very top, like the first example, steering electrode signal drops to zero (Figure 15b) since most of the holes are not trapped and weighting potential is very low. One discrepancy between simulations and measurements is the fall time of the steering electrode signal after electrons are collected by anodes. Fall times of ~ 50 ns are predicted, but instead, ~ 150 ns are observed.

Results of electric field calculations show that for some of the interactions, the electrons can drift to the steering

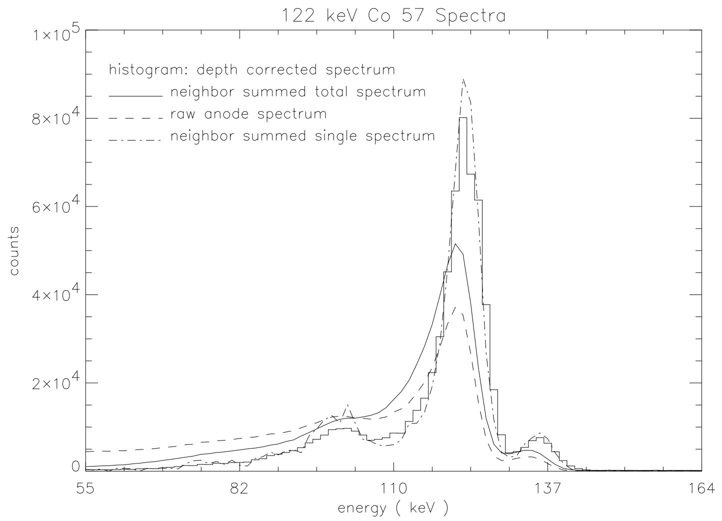

Figure 14. Comparison of depth corrected spectrum (histogram) with uncorrected spectra. Neighbor summed single spectrum is obtained from the top 0.05 mm of the detector. See Section 5.3 for details.

electrodes, or even to the gaps between steering electrodes and anodes. These two cases were modelled also. Fig. 17 shows the case where electrons end up at a steering electrode for an interaction at 0.2 mm. The rise time on the steering electrode signal is greater than that on the anode. The anode signal in this case, rises first and goes down to almost zero since weighting potential is very low at the depths where trapped holes are located. Fig. 17e shows a measured steering electrode signal for Cs^{137} which agrees with the model.

What happens when electrons reach the gaps is unknown. It is modelled with idealized surface conditions for which an electron stops when it reaches the surface. The surface of a semiconductor crystal has a lot of imperfections and therefore has a lot of trap centers for the free charges. Basically, the model treats electrons as trapped when they reach the surface. Fig. 18 shows an example. Both anode and steering electrode do not collect full charge. The steering electrode signal (Fig. 18b) first increases to the maximum as usual, then decrease some, since electrons are directed to the anodes. However. they can not reach the anode, therefore induce a positive signal at the steering electrode. (Compare with the case when electrons reach the anode, the steering electrode signal is negative in this case due to trapped holes.) One of the measurements for the steering electrode showed a similar behavior expected from such interaction (Figure 18e). The timescales and amplitude are consistent with the model. If this interpretation is true, then the electrons move slower very close to the surface and then trapped. The slow increase at greater timescales is due to holes moving away from the steering electrodes.

6. CONCLUSIONS AND FUTURE DIRECTIONS

The model is able to predict correctly the fundamentals of how our detector works. In terms of predicting total signals, it agrees within 1% with the measurements (See Fig. 13). This shows that some parameters that are not included in the program, such as diffusion, and range of photoelectron do not affect the performance of the detector very much. In terms of temporal behavior, the model is within 10% –20% when parameters that are usually found in literature are used. The discrepancies may be due to pulse shaping of electronics or detrapping which was observed for the planar detector. (See section 5.1.)

Trajectory and weighting potential calculations helped us to understand the improvement obtained with adding steering electrode to the system. It is also shown that, the small pixel effect is a result of not only the size of the electrode, but also the distance between electrodes (See Fig. 7). With this in mind, an optimized geometery for enhancing the small pixel effect was studied. In this geometry, anodes are 50 μm wide and steering electrodes are 250 μm wide. Pitch size is 500 μm. More bias is applied between steering electrodes and anodes in order to decrease trajectories ending at wide steering electrodes. Preliminary model results showed an increase from 85% to $> 90\%$ in relative anode signal for very deep interactions compared to detector used now. A detector with this design will be tested later this year.

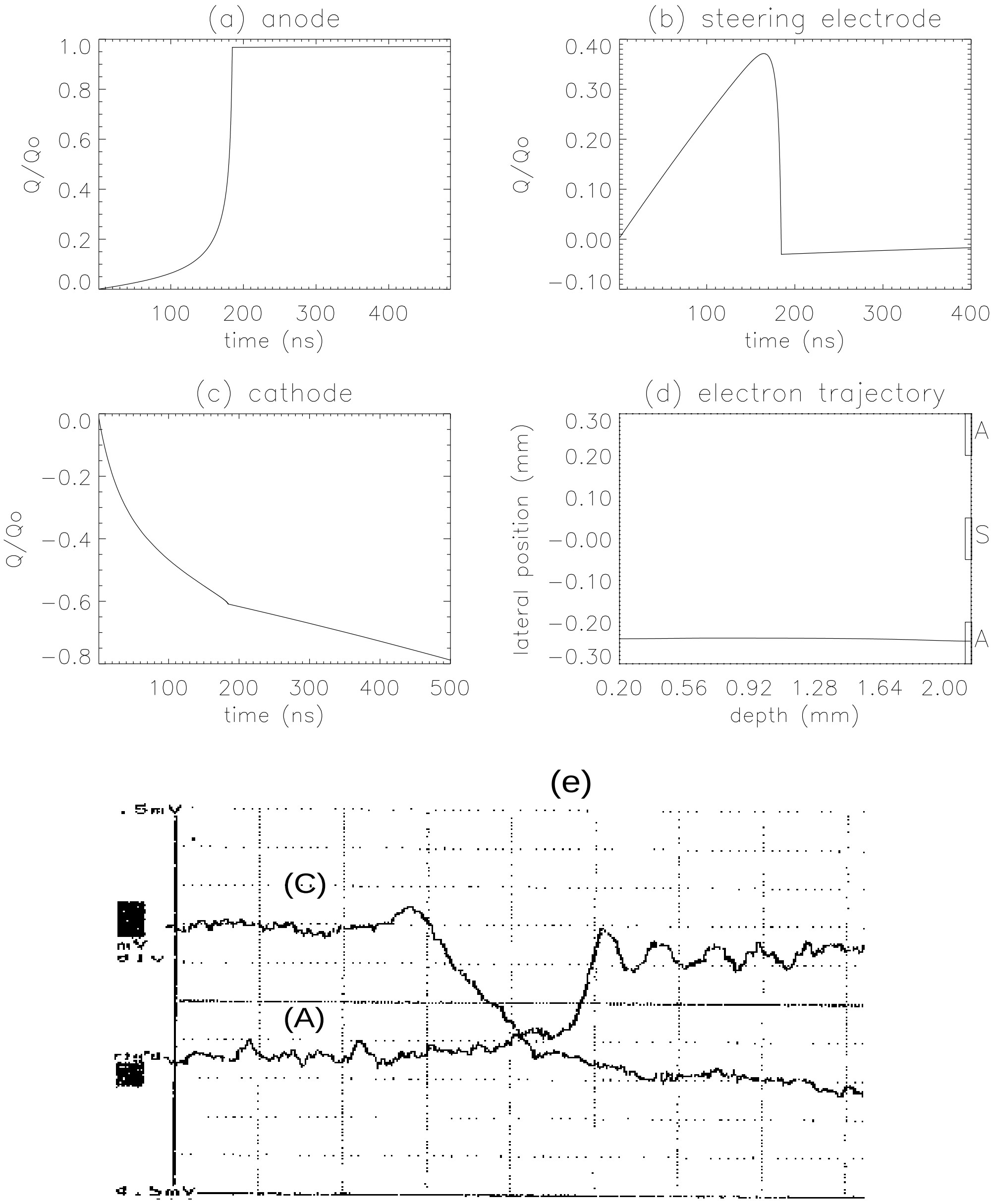

Figure 15. Modelled, (a)-(c), and measured waveforms, (e), and modelled trajectory, (d), for an interaction at 200 μm depth. In (e), the cathode (C) gain is 1.67 times the anode (A) gain. The x-axis unit is 100 ns per division and y-axis unit is 1 mV per division. The overshoot and ringing of anode signal is due to preamlifier response to the short risetime of the signal. See Sect. 5.4 for details.

Both cathode and steering electrode signals are strongly depth dependent. Depth of interaction information, which can be obtained using the model, can be used to reject background[21] and to improve the energy resolution, as demonstrated in this paper.

The model will be improved by adding a Monte-Carlo code to simulate X-ray interactions in the detector. Detrapping and modelling of electronics will also be included. Signals obtained from each interaction will be used to build a spectrum, so that the model will be able to predict the energy resolution of detectors with different geometries and biasing schemes for the electrodes.

The predictions of trajectory calculations will be tested by localizing the X-ray interaction with a 30μm collimated beam which is positioned by a precision X-Y stage.[4] In particular, this will allow us to study the case when electrons

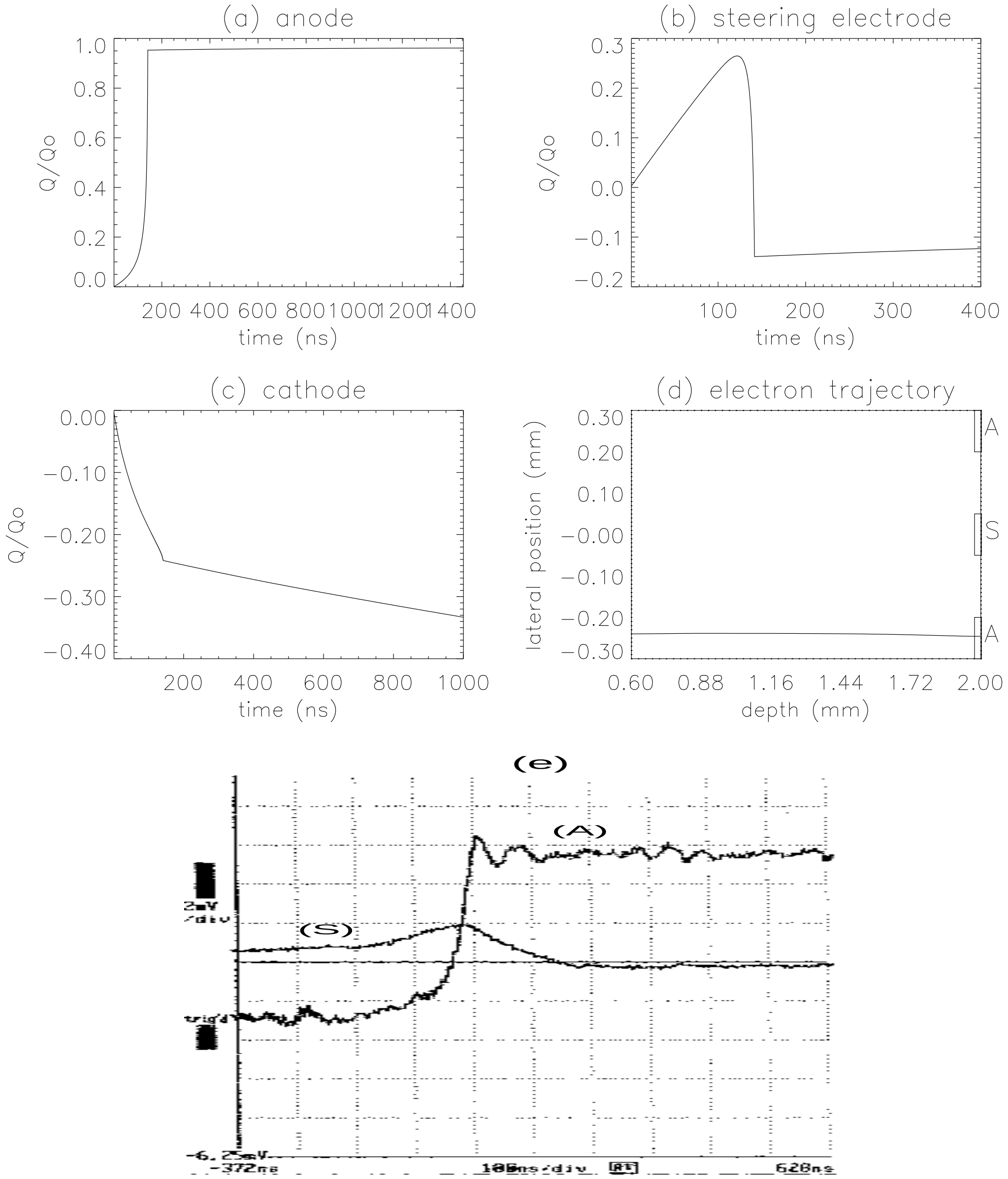

Figure 16. Modelled, (a)–(c), and measured waveforms, (e), and modelled trajectory, (d), for an interaction at 600 μm depth. In Fig. (e), the steering electrode (S) gain is 1.67 times the anode (A) gain. The x-axis unit is 100 ns per division and y-axis unit is 2 mV per division. See Sect. 5.4 for details

reach the gap.

More experiments will be done on planar detector to understand the transport properties, especially detrapping. Homogeneity of the material will be studied by using the collimated beam.

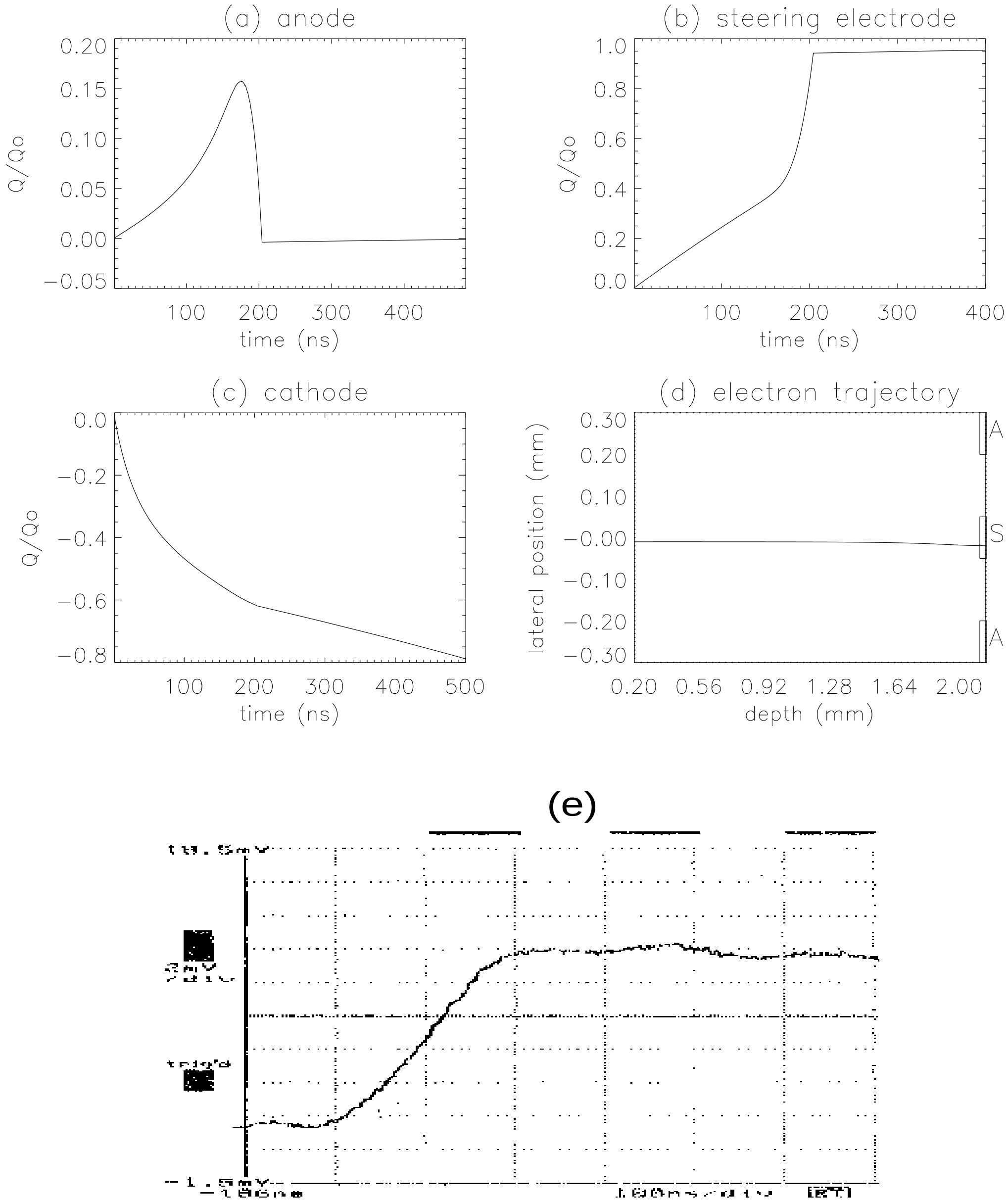

Figure 17. Modelled, (a)–(c), and measured, (e), waveforms and trajectory, (d), for an interaction in which electrons drift to steering electrodes. The depth is 200 μm. In (e), the x-axis is unit 100 ns per division and y-axis unit is 2 mV per division. Events ending on the surface of steering electrodes constitue $\sim$ 10% of all interactions. See Sect. 5.4 for details.

ACKNOWLEDGMENTS

This work was supported by NASA SR&T Grant NAG5-5111 and at WU by NASA SR&T Grant NAG5-5114 and NASA GRSP Grant NGT-50170. Technical support was provided at UCSD by Fred Duttweiler, George Huszar, Charles James, Sandy O'Brien, Phillippe Leblanc, David Malmberg, Ron Quillan and Ed Stephan, and at Washington University by Paul Dowkontt, John Epstein, and Garry Simburger. We would also like to thank to Pat Lamers at Ansoft for providing MAXWELL. Emrah Kalemci was partially supported by TUBITAK.

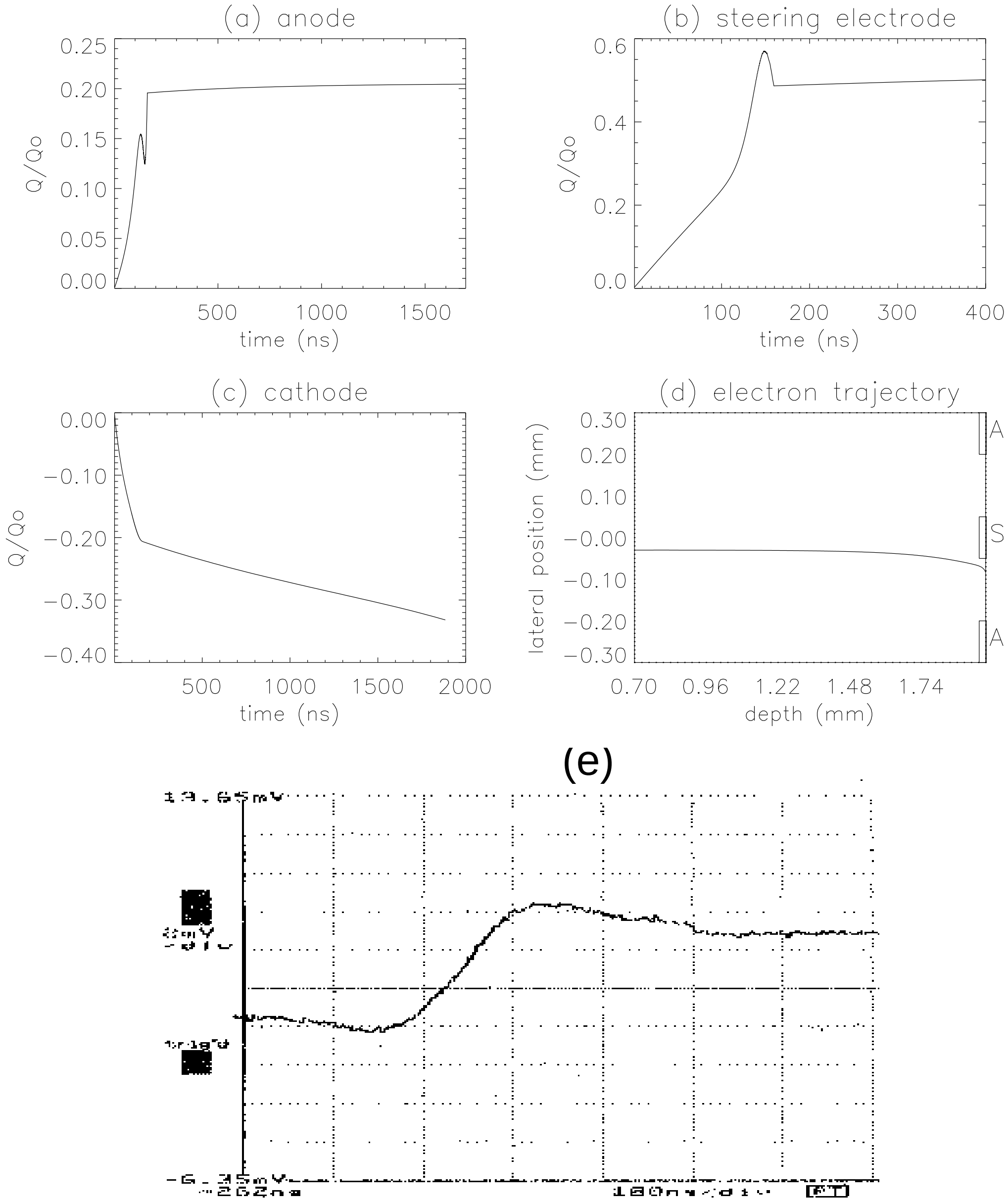

Figure 18. Modelled waveforms, (a)–(c), and trajectory, (d), for an interaction at a depth of 700 μm. In this case, electrons never reach the anode, but collect in the gap. Fig. 17e is a measured waveform which appears to be a gap event. The x-axis unit is 100 ns per division and y-axis unit is 2 mV per division. See Sect. 5.4 for an extended discussion.

REFERENCES

1. 15 Year Plan for X-ray Astronomy, 1994-2008, Report of the X-ray Astronmy Program Working Group, NP-213, NASA Headquarters, High Energy Astrophysics Branch, 1994.
2. J. L. Matteson, F. Duttweiler, G. L. Huszar, P. C. Leblanc, R. T. Skelton, E. A. Stephan, P. L. Hink, P. W. Dowkontt, K. R. Slavis, T. O. Tumer, and S. D. Kravis, "Position-sensitive CZT detector module," in *Hard X-Ray and Gamma-Ray Detector Physics and Applications*, F. P. Doty, ed., *Proc. SPIE* **3446**, pp. 192–203, 1998.

3. J. L. Matteson, W. Coburn, F. Duttweiler, W. A. Heindl, G. L. Huszar, P. C. Leblanc, M. R. Pelling, L. E. Peterson, R. E. Rothschild, R. T. Skelton, P. L. Hink, and C. Crabtree, “CdZnTe arrays for astrophysics applications,” in *Hard X-Ray and Gamma-Ray Detector Physics and Applications*, R. B. Hoover and F. P. Doty, eds., *Proc. SPIE* **3115**, pp. 160–175, 1997.
4. J. L. Matteson, W. Coburn, F. Duttweiler, T. Gasaway, W. A. Heindl, P. C. Leblanc, D. R. MacDonald, M. R. Pelling, L. E. Peterson, R. E. Rothschild, R. T. Skelton, P. Hink, and C. Crabtree, “CdZnTe strip detectors for high-energy x-ray astronomy,” in *Hard X-Ray / Gamma-Ray and Neutron Optics, Sensors, and Applications*, R. B. Hoover and F. P. Doty, eds., *Proc. SPIE* **2859**, pp. 58–73, 1996.
5. H. H. Barret, J. D. Eskin, and H. B. Barber, “Charge transport in arrays of semiconductor gamma-ray detectors,” *Phys. Rev. Lett.* **75,1**, pp. 156–159, 1995.
6. P. N. Luke, “Electrode configuration and energy resolution in gamma-ray detectors,” in *Proceedings of the 9th International Workshop on Room Temperature Semiconductor X- and Gamma-Ray Detectors, Associated Electronics and Applications*, *Grenoble, France* , 1995.
7. J. L. Matteson, D. E. Gruber, W. A. Heindl, M. R. Pelling, L. E. Peterson, R. E. Rothschild, R. T. Skelton, P. Hink, K. R. Slavis, and W. R. Binns, “High energy x-ray imaging spectrometer - HEXIS,” in *EUV, X-Ray, and Gamma-Ray Instrumentation for Astronomy IX*, *Proc. SPIE* **3445**, pp. 445–457, 1998.
8. P. Doty, Personal Communication.
9. Z. He, G. F. Knoll, D. K. Wehe, and Y. F. Du, “Direct measurement of electron drift paramneters using depth-sensing single-carrier CdZnTe detectors,” in *Semiconductors for Room-Temperature Radiation Detector Applications II*, *Mat. Res. Soc. Symp. Proc.* **487**, pp. 89–94, 1997.
10. Y. Eisen and A. Shor, “CdTe and CdZnTe room-temperature x-ray and gamma-ray detectors and imaging systems,” in *Semiconductors for Room-Temperature Radiation Detector Applications II*, *Mat. Res. Soc. Symp. Proc.* **487**, pp. 129–146, 1997.
11. O. Tousignant, L. A. Hamel, J. F. Courville, J. Macri, M. Mayer, M. L. McConnell, and J. M. Ryan, “Transport properties and performance of CdZnTe strip detectors,” *IEEE Trans. on Nucl. Sci.* **45, 3**, pp. 556–560, 1998.
12. G. F. Knoll, *Radiation Detection and Measurement*, John Wiley & Sons, New York, 1979.
13. P. N. Luke and E. E. Eissler, “Performance of CdZnTe coplanar-grid gamma ray detectors,” *IEEE Trans. on Nucl. Sci.* **43, 3**, p. 1481, 1996.
14. M. Martini and T. A. McMath, “Trapping and detrapping effects in lithium-drifted germanium and silicon detectors,” *Nucl. Instr. and Meth.* **79**, pp. 259–276, 1979.
15. J. W. Mayer, “Semiconductor materials for gamma-ray spectroscopy,” in *Semiconductor Detectors*, G. Bertolini and A. Coche, eds., pp. 445–496, John Wiley & Sons, New York, 1968.
16. S. Ramo, “Currents induced by electron motion,” *Proc. I.R.E.* **27**, pp. 584–585, 1939.
17. K. Hecht, “Zum mechanismus des lichtelektrischen primarstromes in isolierenden,” *Z. Physik* **77**, p. 235, 1932.
18. L. A. Hamel, J. R. Macri, C. Stahle, J. Odom, F. Birsa, P. Shu, and F. Doty, “Signal generation in CdZnTe strip detectors,” *IEEE Trans. on Nucl. Sci.* **43, 3**, pp. 1422–1426, 1996.
19. MAXWELL, *A Software to Solve Electromagnetic Problems*, ANSOFT, Four Station Square, Suite 660, Pittsburgh, PA 15219 USA.
20. M. L. Cherry, D. L. Band, J. Buckley, T. G. Guzik, P. Hink, J. R. Macri, J. L. Matteson, M. L. McConnell, T. J. O'Neill, J. M. Ryan, J. G. Stacy, and A. D. Zych, “MARGIE: An ultra-long duration balloon instruent for wide-field- of-view high-angular-resolution hard x-ray astronomy,” in *EUV, X-Ray, and Gamma-Ray Instrumentation for Astronomy X*, *Proc. SPIE* , 1999.
21. K. Slavis, P. Dowkontt, F. Duttweiler, J. Epstein, P. L. Hink, G. L. Huszar, P. Leblanc, J. L. Matteson, R. T. Skelton, and E. Stephan, “High altitude balloon flight of CdZnTe detectors for high energy x-ray astronomy,” in *EUV, X-Ray, and Gamma-Ray Instrumentation for Astronomy IX*, *Proc. SPIE* **3445**, pp. 169–184, 1998.
22. Z. He, G. F. Knoll, D. K. Wehe, and J. Miyamoto, “Position-sensitive single carrier CdZnTe detectors,” *NIM A* **388**, pp. 180 – 185, 97.